

Hydrodynamic Backflow for Easing the Fermion Sign in Finite-Temperature Electron Path Integral Simulations

Ingvars Vitenburgs

*Department of Chemistry, Imperial College London,
South Kensington Campus, London, SW7 2AZ, UK.*

Jarvist Moore Frost*

*Department of Chemistry, Imperial College London,
South Kensington Campus, London, SW7 2AZ, UK. and
Department of Physics, Imperial College London,
South Kensington Campus, London, SW7 2AZ, UK.*

(Dated: April 3, 2026)

Some notable systems, such as room-temperature superconductors and materials for controlled nuclear fusion, require an accurate description of finite-temperature quantum matter. Stochastic path integral methods are finite-temperature and numerically exact, but scale poorly with system size due to the notorious Fermion sign problem. To somewhat mitigate this, we use a hydrodynamical backflow coordinate transformation. Our first attempt was a continuous normalizing flow machine learning approach to determine the optimal parameters. We found this to reduce the error of the total energy, approximately, three times at medium sign severity. Numerical issues challenged training effectively. Thus, a semi-analytic approach was developed to estimate the optimal parameters. We do this by using a derived expression dependent on a Bosonic observable. Hence, the calculation of these values does not have a sign problem. The resulting backflow transformations reduce the problem by multiple orders of magnitude, specifically, in the case of a harmonically trapped, two-dimensional electron gas at finite-temperature. The total energy of the system agrees with previous, backflow untransformed, studies and we calculate energies for up to 32 electrons. The limiting factor is found to be, primarily, the $O(N^3)$ calculation of the Jacobian, stemming from the coordinate transformation of the backflow. A more thorough implementation may further improve this scaling. Otherwise, a pathway for simulating electron systems at currently unreachable regimes is obtained. Finally, as a specific practical use case in energy storage systems, the quantum capacitance for graphene quantum dot materials is calculated.

I. INTRODUCTION

Accurate numerical solution of the Schrödinger equation is at the centerpoint of modern development of materials and molecules. All exact methods fundamentally scale factorial in the number of electrons. In stochastic methods based upon Monte-Carlo integration, this scaling appears as the Fermion sign problem, where taking the arithmetic mean of an increasingly oscillatory integrand leads to an exploding variance.

Stochastic path integral methods are finite-temperature and numerically exact, but scale poorly [1] with system size due to the Fermion sign problem. Some notable technical systems, such as room-temperature superconductors [2] and materials for controlled nuclear fusion [3], require such an accurate description of finite-temperature quantum matter.

In recent decades, stochastic path-integral methods for Fermionic matter have been relatively neglected. Recent algorithmic improvements for Bosonic matter [4] and extrapolation from Bosonic to Fermionic matter via a fictitious non-integer sign [3, 5] have led to increased recent interest. Simultaneously, machine-learning approaches

which offer a more sophisticated trial wavefunction [6–9] have been developed.

We apply the most simple (hydrodynamical) backflow coordinate transformation [10] to a finite temperature path integral molecular dynamics simulation of electrons.

$$\tilde{\mathbf{r}}(\mathbf{r}) = \mathbf{r} + \sum_{\mathbf{r}_i \neq \mathbf{r}} A \frac{\mathbf{r} - \mathbf{r}_i}{1 + \left(\frac{|\mathbf{r} - \mathbf{r}_i|}{l}\right)^3}. \quad (1)$$

Here, we move from the particle position to a quasi-position based on a transformation with a strength A and a backflow decay length of l . Though this backflow has a simple closed-form, it has been shown to reduce the errors in zero temperature electron gas simulations [11]. We came across it in the context of its use in describing asymptotic behaviour of the Fermi liquid when modelling non-interacting Fermions [12].

Starting with the open-source path-integral molecular-dynamics (PIMD) code of Xiong and Xiong [5], we develop two methods to optimise the parameters of this backflow transformation to minimise the sign error in a finite temperature electron simulation.

Chronologically, our first approach was based on a neural ordinary differential equation representation of the transform [13], but we found this fragile and numerically unstable. Our second approach directly optimises the

* jarvist.frost@imperial.ac.uk

backflow parameters using a gradient from a closed-form solution for the linear correction. Whilst such an approach has been studied before [14], it was not as generally applicable as here and composed of quite a few approximations. We compare to a traditional approach of gradient-free optimisation, and plot the average sign on a grid of backflow parameters.

We demonstrate the method on a two-dimensional electron gas in a harmonic trap at finite-temperature with reference data provided by Dornheim [15]. In addition, it is found that the backflow wavefunction offers a significant improvement in the average sign at finite temperature.

Finally, as an example for where such an abstract system can be applied to practical material design, we calculate the quantum capacitance [16, 17] of graphene quantum dots [18, 19], a system of interest in supercapacitors and batteries.

II. HYDRODYNAMIC BACKFLOW IN PATH INTEGRAL MOLECULAR DYNAMICS

The computational cost of sampling the Fermionic wavefunction has exponential scaling due to the alternating sign in the estimator [1], a fundamental property of Fermion exchange, $\psi(\dots, r_1, \dots, r_2, \dots) = -\psi(\dots, r_2, \dots, r_1, \dots)$. For Bosonic systems the sign does not change under exchange, and therefore Monte-Carlo estimators converge well. Recently, an approach has been developed based on a fictitious partial sign [3, 5] which extrapolates the behaviour from Boson to sign-free Boltzmann into the Fermion regime. However, these are interpolation based approaches: efforts to reduce the Fermionic sign problem would still be of use in allowing you to collect more unbiased data-points from the Fermionic region.

Our work is motivated by the observation that the sign problem grows as a function of inverse temperature (also particle number; interaction strength), and that the complexity of the nodal surface [12] grows as a function of the backflow strength. Rather than directly try and learn the ground-state wave-function, would it be more computationally tractable to learn the development of nodal complexity along the non-interacting to fully-interacting system.

We therefore want to gradually learn a general coordinate transformation $\tilde{\mathbf{r}}(\mathbf{r})$ corresponding to the least noisy average phase $\langle\sigma\rangle$ value, required for calculating any observable, an individual sample of which is defined as

$$\sigma = \frac{\int \prod_i d\mathbf{r}_i |J[\{\tilde{\mathbf{r}}(\mathbf{r}_i)\}]| e^{-S[\{\tilde{\mathbf{r}}(\mathbf{r}_i)\}]}{\int \prod_i d\mathbf{r}_i |J[\{\tilde{\mathbf{r}}(\mathbf{r}_i)\}]| |e^{-S[\{\tilde{\mathbf{r}}(\mathbf{r}_i)\}]}|}. \quad (2)$$

Here $S[\{\tilde{\mathbf{r}}(\mathbf{r}_i)\}]$ is the action, required in the Metropolis-Hastings algorithm for stochastic sampling and $J[\{\tilde{\mathbf{r}}(\mathbf{r}_i)\}]$ is the Jacobian. It is trivial to see that the property

$e^{a+ib} = e^{ib}|e^{a+ib}|$ is used in Eq. 2 to sample the imaginary phase, which is needed to correct the observables, since this has been infused into them via $\langle O \rangle \rightarrow \langle O e^{ib} \rangle$ for the Metropolis-Hastings algorithm to even be applicable. Note that, if there is no sign problem present, as in the cases mentioned above, the average sign $\langle\sigma\rangle$ approaches unity.

Previous work [20–22] shows that there exists such an upper limit of this phase, corresponding to the best possible contour - here $\tilde{\mathbf{r}}(\mathbf{r}_i)$ described - representation of the system. Nevertheless, these studies focus primarily on primitive quantum field theory models at most, used in some particle physics theories. Transformations are shown to house Lefschetz thimbles (function $f(x)$ poles in a general coordinate $\tilde{x} = x + f(x)$ transformation) for easing the sign problem and here we make a connection to many-electron systems via the backflow in Eq. 1. We believe that applying such transformation will alter the stochastic sampling by skewing towards regions with either of the possible sign values.

A. Computational details

Using an already available implementation [5, 23] of an exact stochastic path integral ring polymer molecular dynamics formalism, it is possible to generate learning data $\{\mathbf{r}_i(\sigma, T)\}$ and find a suitable transformation for maximizing the average phase $\langle\sigma\rangle$, defined in Eq. 2. This is done by inferring a coordinate transformation, consisting of multiple hydrodynamical backflow functions, already present in the data.

As a test case, the approach developed here is applied to a system with an already available implementation - the two dimensional harmonic trap with a Coulomb interaction. The Hamiltonian for this system is given by

$$H = -\sum_i \nabla_i^2 + \sum_i \mathbf{r}_i^2 + \sum_{i<j} \frac{\gamma}{|\mathbf{r}_i - \mathbf{r}_j|}. \quad (3)$$

Here the energy scales are expressed in terms of half of the oscillator energy $\hbar\omega$, which effectively describes the width of the trap, and a $\sqrt{\frac{\hbar}{m\omega}}$ length scale. It is known [24] that even at medium coupling γ and temperature T regimes the sign problem is quite significant. PyTorch [25] was used on top of the open-source Xiong and Xiong [5] PIMD code.

The parameters used for these test case simulations were identical to the ones used in the study [5] of the stochastic path integral ring polymer molecular dynamics formalism itself - a total of $5 \cdot 10^6$ steps of $h = 0.0025$ time increment, simulating four particles at $T = 1.0$ temperature, described by the Hamiltonian in Eq. 3 with $\gamma = 1.0$ coupling.

The codes used to produce the results reported in this paper are available on GitHub [26].

B. Parameters by a neural network optimisation

Machine learning techniques have been applied with some success [27, 28] by representing the high-dimensional ground-state wavefunction as a neural network, optimised variationally, and thereby significantly improve the accuracy of variational Monte-Carlo calculations for small molecules and simple periodic materials. Recently [6–9] the continuous normalizing flow method [13] has been shown to be able to solve a few simple quantum many-body systems in their ground states as well.

This approach has the advantage of inferring the solution, in part, via some form of a differential equation, thus being much easier to analyse analytically, rather than resulting in a black-box situation like general neural network [28] approaches. In this case, the dynamic of a single point $\mathbf{r}(\sigma, T)$ of some distribution $p[\mathbf{r}(\sigma, T)]$, with respect to the sign value σ , can be expressed via a representation function set $\{f_n\}$ with

$$\frac{d\mathbf{r}(\sigma, T)}{d\sigma} = \sum_n f_n(\mathbf{r}(\sigma, T)). \quad (4)$$

Moreover, this formalism is designed to be, specifically, applied to probability distributions, hence, simplifying the calculation, and has been discussed to be suitable [29] to quantum many-body wavefunctions as well. In this case, the evolution of the probability distribution can be shown to yield

$$\frac{d \log(p[\mathbf{r}(\sigma, T)])}{d\sigma} = \sum_n \text{Tr} \left(\frac{\partial f_n}{\partial \mathbf{r}} \right). \quad (5)$$

This can be further used in a cost function, after integrating over σ , to perform maximum likelihood estimation between the model in Eq. 4 and the data $\{\mathbf{r}_i(\sigma, T)\}$ with respect to parameters of the $\{f_n\}$ representation function set.

Previous continuous normalizing flow approaches for solving quantum many-body systems, discussed above, struggle to choose an appropriate f_n in Eq. 4 that doesn't constrain the amount of nodes - spatial manifolds where the wavefunction changes sign. Additionally, it has been proposed [10, 11] that the properties of hydrodynamical backflow effects can be an appropriate, meaning general enough, way of describing nodal surfaces in Fermion systems. More specifically, they have been studied to house a very rich, fractal nodal structure, with a changing amount of nodes. These backflow forms have also been shown [30] to stabilise variational and diffusion quantum Monte-Carlo studies. They are characterized by a plane wave, $\phi(\mathbf{k}_n) \sim e^{i\mathbf{k}_n \cdot \mathbf{r}}$, expansion in momentum space, corresponding to a point $\{\mathbf{r}_i\}$ distribution $|\phi(\mathbf{r}_n)|^2 = \sum_n \delta(\mathbf{r} - \mathbf{r}_n)$ in coordinate space, converted by the use of a Fourier transform and shifted by collectively

dependent motion. Here $\mathbf{k}_n = \sum_{i=\{x,y,z\}} \frac{\pi n_i}{L} \hat{\mathbf{i}}$ is the discretized momentum, within a $\{x_n, y_n, z_n\} \in [-\frac{L}{2}, \frac{L}{2}]$ infinite potential box, and $\delta(x)$ is the Dirac delta function. The real space representation can be derived, as an example in one dimension, r , by starting from the discrete Fourier transform \mathcal{F}_d with

$$\begin{aligned} \phi(r) &= \mathcal{F}_d[e^{ik_n r}] = \\ &= \sum_{j=1}^{\infty} e^{i \frac{2\pi j}{L} r} e^{-i \frac{2\pi j}{L} r_0} \rightarrow \frac{1}{L} \delta\left(\frac{r_0 - r}{L}\right). \end{aligned} \quad (6)$$

Moving on, the collectively dependent motion coordinate transformations are introduced via $\{f_n\}$ in Eq. 4 and yield

$$\begin{aligned} \tilde{\mathbf{r}}(\mathbf{r}) &= \mathbf{r} + \sum_n \int_{\sigma_0}^{\sigma} f_n(\mathbf{r}(\sigma, T)) d\sigma = \\ &= \mathbf{r} + \sum_{n, \mathbf{r}_i \neq \mathbf{r}} \frac{\mathbf{r} - \mathbf{r}_i}{1 + \left(\frac{|\mathbf{r} - \mathbf{r}_i|}{l_n(T)}\right)^3} \int_{\sigma_0}^{\sigma} a_n(\sigma, T) d\sigma. \end{aligned} \quad (7)$$

Here σ_0 is the average phase corresponding to distribution data $\{\mathbf{r}_i(\sigma_0, T)\}$ when no coordinate transformation has been applied - $\tilde{\mathbf{r}}(\mathbf{r}) = \mathbf{r}$ and $\int_{\sigma_0}^{\sigma} a_n(\sigma, T) d\sigma = 0$. It can also be seen that it is more useful to represent the integral $\int_{\sigma_0}^{\sigma} a_n(\sigma, T) d\sigma = A_n(\sigma, T)$ as a neural network rather than the $a_n(\sigma, T)$ function itself. Hence, the backflow strengths $\{A_n(\sigma, T)\}$ and length scales $\{l_n(T)\}$ are neural networks describing the nodal surface structure of the Fermionic system and are learned by averaging over individual samples. Furthermore, the summation is over all of the other particle coordinate points $\{\mathbf{r}_i(\sigma_0, T)\}$ at the same imaginary time step - bead number, in stochastic path integral terminology - of the untransformed distribution. While there are [31] more sophisticated forms of backflow transformations, their use would make the analysis too complex, whilst not giving a much better representation of the effects under question. In combination with Eq. 5 this yields a cost function $\sum_i \log(p[\mathbf{r}_i(\sigma, T)])$ for performing maximum likelihood estimation on $\{\mathbf{r}_i(\sigma, T)\}$ data where

$$\log(p([\mathbf{r}(\sigma, T)])) = \int_{\sigma_0}^{\sigma} \sum_n \text{Tr} \left(\frac{\partial f_n}{\partial \mathbf{r}} \right) d\sigma. \quad (8)$$

Here the probability distribution of the simulation data $\log(p([\mathbf{r}(\sigma_0, T)]))$ has been neglected in the expression, since it is just a scaling constant and doesn't impact the optimization process, due to being just the prior in Bayes theorem.

The details of this process is given in App. A with the main result depicted in Fig. 1 - the learned optimal sign backflow strength and length scale values of a single backflow match the global maximum from direct sampling of these values. An $0.2 \rightarrow 0.5$ average sign $\langle \sigma \rangle$ value increase is yielded with a multiple of applied backflows not gaining any improvement.

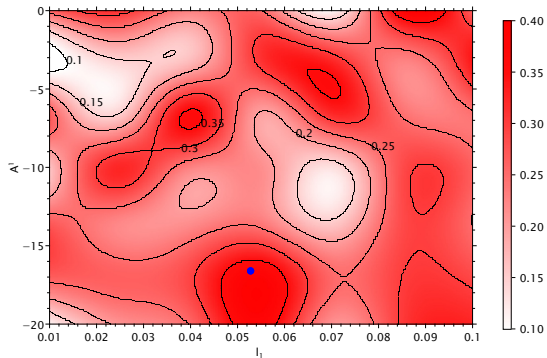


FIG. 1. Direct grid sampling of the average sign with respect to the length and strength scales of a single applied backflow. The blue dot denotes maxima obtained by the machine learning approach.

C. Semi-analytical optimisation of backflow transforms

It is believed that the instabilities, detailed for the learning process above in App. A, would constitute the implementation of such a real-time machine learning algorithm, on top of any path integral Monte-Carlo or molecular dynamics code, difficult. Hence, it is worth turning to a semi-analytical description of the sampling behaviour for this approach, in order to search for an alternative way to find the best backflow parametrization. It is convenient to start with the two-particle case in one dimension. The wavefunction of this Fermion system, with an applied backflow and centred at the origin, is defined by

$$\psi(x_1, x_2) = \begin{vmatrix} e^{ik_1 \left(x_1 + A \frac{|x_1 - x_2|}{1 + \frac{|x_1 - x_2|^3}{l^3}} \right)} & e^{ik_1 \left(x_2 + A \frac{|x_2 - x_1|}{1 + \frac{|x_2 - x_1|^3}{l^3}} \right)} \\ e^{ik_2 \left(x_1 + A \frac{|x_1 - x_2|}{1 + \frac{|x_1 - x_2|^3}{l^3}} \right)} & e^{ik_2 \left(x_2 + A \frac{|x_2 - x_1|}{1 + \frac{|x_2 - x_1|^3}{l^3}} \right)} \end{vmatrix}. \quad (9)$$

Here A and l are the strengths and lengths of a single backflow transformation, as discussed previously. The discretized momentum $k_i = \frac{2\pi n_i}{L}$ with $n_1 < n_2$ and $n_1, n_2 \in \mathbb{Z}$ represents a periodic box with the unit cell at $x \in [-\frac{L}{2}, \frac{L}{2}]$. Since, the calculation above in Sec. II B yielded a very small length l value, the linear - short-range - approximation, with respect to the expansion coefficient $l^3 \ll 1$, can be used. This results in an adjustment of $1 + \left(\frac{x_1 - x_2}{l}\right)^3 \approx \left(\frac{x_1 - x_2}{l}\right)^3$ to the wavefunction, producing the linear correction of the wavefunction, $\psi(x_1, x_2) = \psi_0(x_1, x_2) + \psi_1(x_1, x_2)$, where $\psi_0(x_1, x_2)$ is the unperturbed - null, $l \rightarrow 0$, backflow - case. This, specifically first-order case, corresponds to the form used by Feynman [10] to describe correlations in He^4 and since been analytically studied [12] to produce up to two-particle interactions.

The corresponding energy can be then derived to be

$$E_0 + E_1 = k_1^2 + k_2^2 + i \underbrace{\frac{2Al^3(3 - 2\gamma_E)}{L^2}}_{\text{Exchange term}} (k_1 - k_2)^2 (k_1 + k_2). \quad (10)$$

Here γ_E is the Euler-Mascheroni constant (≈ 0.5772) and the convention $n_2 > n_1$ was used to simplify the algebra. Note that the imaginary unit is present due to the fact that the switch to imaginary time, as is done usually in path integral algebra, has yet not been done. It is also trivial to see that the exchange term flips its sign in the Boson case, where the determinant in Eq. 9 is replaced by a permutant. A further calculation of the sign, defined [5] as the exponentiated imaginary difference between the Boson E_b and Fermion E_f energies, after a Fourier transform to coordinate space, similar to the procedure in Eq. 6, and extension to the many-particle and two-dimensional case, yields

$$\begin{aligned} \mathcal{R}(\sigma) &= \mathcal{R} \left[\frac{e^{i\beta(E_b - E_f)}}{i} \right] \rightarrow \\ &\rightarrow -\sin \left(\frac{Al^3\beta(3 - 2\gamma_E)}{4\pi^2} \times \right. \\ &\left. \times \sum_{i \leq j} \left[\frac{2|\mathbf{r}_j|^3 + 2|\mathbf{r}_i|^3 + |\mathbf{r}_j - \mathbf{r}_i|^2 |\mathbf{r}_j + \mathbf{r}_i|}{|\mathbf{r}_j|^4 |\mathbf{r}_i|^4} \right] \right). \end{aligned} \quad (11)$$

Note that the presence of stand-alone coordinates is due to the plane-wave system being centred at the origin.

It is interesting to see that the final expression is independent of the hard-confinement length L . To calculate any higher order - more long-range - energy corrections, perturbation theory can be used by expanding with respect to the expansion coefficient l^3 . More specifically, the effects of the backflow can be interpreted as a perturbation δH without actually deriving its analytical expression. As it is obvious that such an algebraic manipulation would most probably not yield a useful form for physical understanding of the underlying processes, it is more efficient to use some ideas from the recursive approach [32]. In this case a low order approximation, such as the one derived in Eq. 11 above, is applied multiple times to further optimize the nodal surface sampling. More specifically, the ideal, meaning least noisy, wavefunction samples are taken when $\langle \sigma \rangle = 1$ in Eq. 11 and, hence, the condition for Al^3 can be shown to be

$$\begin{aligned} \langle Al^3 \rangle &= \left\langle -\frac{2\pi^3}{\beta(3 - 2\gamma_E)} \times \right. \\ &\left. \times \left(\sum_{i \leq j} \frac{2|\mathbf{r}_j|^3 + 2|\mathbf{r}_i|^3 + |\mathbf{r}_j - \mathbf{r}_i|^2 |\mathbf{r}_j + \mathbf{r}_i|}{|\mathbf{r}_j|^4 |\mathbf{r}_i|^4} \right)^{-1} \right\rangle. \end{aligned} \quad (12)$$

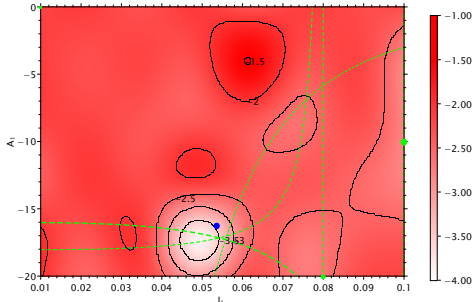


FIG. 2. Direct grid sampling for searching the optimal backflow parameters with respect to the length and strength scales of a single applied backflow. Specifically, the quantity $\log|\delta A l^3| = |\langle \tilde{A} l^3 \rangle - A l^3|$ is plotted. The intersection of the green lines, depicting the solution of the analytical approach, sampled at the three green dots, is also shown. The blue dot represents the machine learned optimal parameters value from Fig. 1.

As an initial test, this value can be calculated for the system studied previously. Hence, a measurement of this observable at the point $\{A = -15.83, l = 0.05374\}$, predicted by the machine learning approach, converged in the same fashion as in Fig. 8 and yielded an estimate of $\langle \tilde{A} l^3 \rangle = -2.6 \cdot 10^{-3} \approx A l^3 = -2.4 \cdot 10^{-3}$ with both being quite close to each other. Thus, it is possible to interpret this as a solved recursive problem - formula in Eq. 12 suggests that the optimal, meaning least noisy, sampling happens at the backflow parameterization values that this observable is being sampled at, hence signalling convergence. The relatively minor deviation is most likely caused from the first-order approximation nature, as well as the numerical deviations of the machine learning algorithm in combination with the cubic sensitivity of l . To further confirm this, direct grid sampling was conducted for the $\log|A l^3 - \langle \tilde{A} l^3 \rangle|$ observable in an identical approach to Fig. 1 at various strength and scale values and is displayed in Fig. 2. It can be immediately seen that there is a global minimum, subject to a small binning deviation, as before, further supporting this statement, where the machine learned results have been depicted by a blue dot. Hence, a sort of a grid search method is produced, where the step value $\delta A l^3 = \langle \tilde{A} l^3 \rangle - A l^3$ with respect to the origin $A l^3$ is known, for finding the optimal backflow parameterization.

It is important to recount that, the calculation of the required observable for this grid search, defined in Eq. 12, does not suffer from the exponentially scaling Fermion sign problem, since the calculation of the sign $\langle \sigma \rangle$ itself - meaning adjustment to Fermi statistics - is not required. In contrast, the addition of a single backflow transformation is estimated to have a polynomial $O(N^3)$ cost scaling, but can be [33] improved by using more efficient algorithms for Jacobian estimation. As an example of the grid search method, in Fig. 2 the magnitudes of the steps

$\delta A l^3$ are evaluated at three A and l values, depicted by green dots, of decreasing width, at $\{A = -20, l = 0.08\}$, $\{A = -10, l = 0.1\}$ and the origin. These were calculated to yield $\delta A l^3 = 1.2 \cdot 10^{-2}$, $\delta A l^3 = -2.5 \cdot 10^{-3}$ and $\delta A l^3 = -6.6 \cdot 10^{-3}$, respectively. The corresponding sets of valid backflow parameter values are then plotted via green dotted lines, again of decreasing thickness, with the intersection denoting the solution. The corresponding line equations for satisfying this condition are found by first-order expansion at the origin via

$$\begin{aligned} \delta(A l^3) &= (\delta A) l^3 + A(\delta l^3) = \\ &= (A - 0) l^3 + A(l^3 - 0) \rightarrow A = \frac{\delta(A l^3)}{2 l^3}. \end{aligned} \quad (13)$$

Furthermore, shifting to non-origin expansion points yields

$$A = \frac{\delta(A l^3)}{2(l^3 - l_0^3)} + A_0. \quad (14)$$

After plotting all three lines, discussed above, it can be immediately seen that this results in an agreement with the values obtained from the machine learning and direct grid sampling approaches. Additionally, the $\delta A l^3$ values not sampled at origin can be seen to yield a closer estimate to the one produced numerically from the machine learning approach, as expected from a first-order approximation.

III. RESULTS

A. Average sign for a finite temperature quantum harmonic oscillator

Studying the Hamiltonian in Eq. 3 is of general interest, as it models trapped strongly correlated electrons, properties of which have been speculated to yield better understanding of some notable systems, such as room-temperature superconductors [2] and materials for controlled nuclear fusion [3], among others.

Hence, the backflow sampling procedure, derived in the last section, is utilized to reach particle number regimes too noisy for current approaches. Now, instead of running 128 simulations with different seeds, only a few are run, with the amount of steps conducted corresponding to just enough to reach convergence for each individual case, as in a practical scenario. The resulting sign and per-particle energy values, with their respective errors, are compared, partially, with a previous study [15] and shown in Fig. 3 and Fig. 4, respectively. Furthermore, it was verified that at the predicted optimal backflow parameters $\delta A l^3 \ll A l^3$ held and it is worth noting that quite often an initial guess around the first curve satisfied this condition already, thus not requiring a second simulation run.

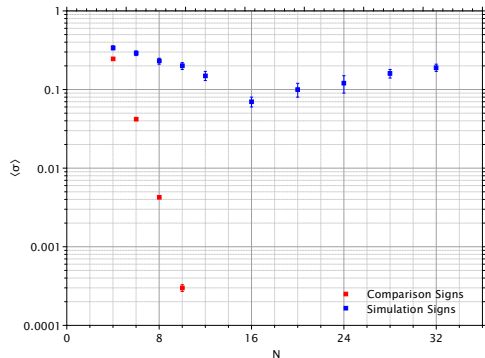


FIG. 3. Sign values (blue dots) with the corresponding errors for different particle numbers from the backflow transformed simulation runs. A partial comparison (red dots) with previous study data of Dornheim [15] with no applied backflow is given as well.

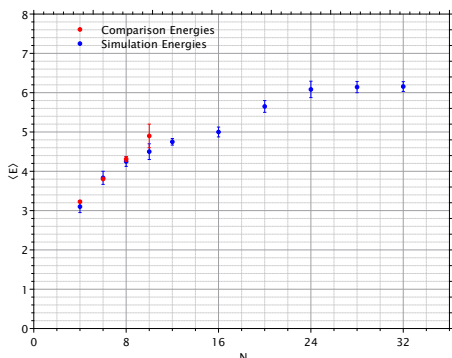


FIG. 4. System per-particle energy (blue dots) with the corresponding errors for different particle numbers from the backflow transformed simulation runs. A partial comparison (red dots) with previous study data of Dornheim [15] with no applied backflow is given as well.

It is immediately visible that the exponential decay of the sign value $\langle \sigma \rangle$ is significantly suppressed, reaching its most severe value of $\sigma = 0.07 \pm 0.01$ at 16 electrons. It is further interesting to note that some kind of a phase transition can be observed around this region, more strongly from the sign dependence, rather than the energy. In fact, the critical particle number for crystallization to a Wigner phase can be estimated via the Lindemann melting criterion [34]. This has been, relatively recently, shown to be valid in two dimensions, not only three, and states that at the critical point the root-mean-square displacement of the electrons $\langle \xi^2 \rangle$ is related to the characteristic interparticle distance a via a $\sqrt{\langle \xi^2 \rangle} \simeq 0.24a$ relation. Estimating $\sqrt{\langle \xi^2 \rangle}$ from simula-

tion energy data in Fig. 4 and length scale used in the Hamiltonian, defined by Eq. 3, yields a value of $N_c \simeq 18$, relatively close to the one predicted by the simulations here, thus suggesting that the bump in Fig. 3 may signify this phase transition.

In addition, to explore the underlying physics a bit further, the power of the two-body interaction is modified in Eq. 3, whilst keeping all of the other parameters fixed, via $|\mathbf{r}_i - \mathbf{r}_j| \rightarrow |\mathbf{r}_i - \mathbf{r}_j|^\alpha$, where $\alpha = 1$ corresponds to the Coulomb case mostly studied here. The effect of this is displayed in Fig. 5 on the sign value and Fig. 6 on the backflow - A and l - parameters. The particle number is set to $N = 6$ as well and, hence, available comparison data [15] is present for the former, with $\alpha = 3$, representative of a dipole-dipole interaction and $\alpha = 0$ to a non-interacting system. It can be immediately seen that the approach developed above is only beneficial for cases with a strong or medium sign problem, basically adding not needed complexity in the weak sign problem case. In all dependencies there is a sort of a change of dependence slope that occurs in the $\alpha \in (1; 2)$ range, possibly indicative of some sort of a phase transition. Interestingly, an increase of the interaction order, which is known to decrease the sign problem, actually makes the algorithm in Eq. 12 predict a stronger backflow. This could be indicative of the two-dimensional backflow parameter grid, one example of which was displayed in Fig. 2, being too smooth, most realistically caused from the gradient being negligible due a significant increase of the σ sign value not being present from variations in A and l values. The actual length scale of the predicted optimal backflow is seen to be constrained within a $l \in (0.05; 0.09)$ range.

Finally, we also vary temperature with the parameterization above and find a significantly reduced sign problem too. This is displayed in Fig. 7. Surprisingly, the magnitude of this effect has quite complex behaviour. The worst performance is present at the high temperature regime - this is though to be caused, as before, from, essentially, introducing noise into a case with no sign problem. There is some sort of a phase transition present, as before as well, at an intermediate temperature case where the mitigation performance of the backflow takes a small dip before recovering as the system becomes colder.

B. Energy storage in quantum dots

The Hamiltonian in the previous subsection effectively models [17] quantum dot systems. More specifically, graphene quantum dots [18] have recently been shown [19] to be a candidate for supercapacitor energy storage applications, among many other use cases. They are used as the electrodes in these systems and form of a few layers of graphene - graphite - with only few unit cells of width. Hence, the total capacitance in these systems can be studied [16] by observing the energy dependence on the amount of accumulated charge - here the amount of

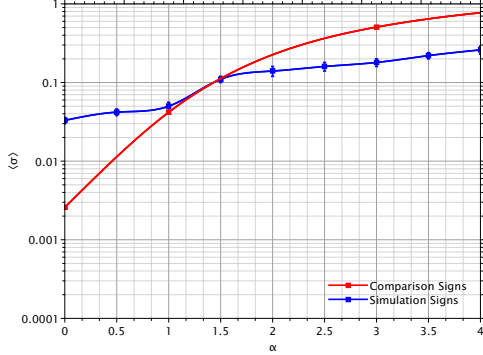


FIG. 5. Sign values (blue dots) with the corresponding errors for different interaction powers from the backflow transformed simulation runs. A partial comparison (red dots) with previous study data of Dornheim [15] with no applied backflow is given as well.

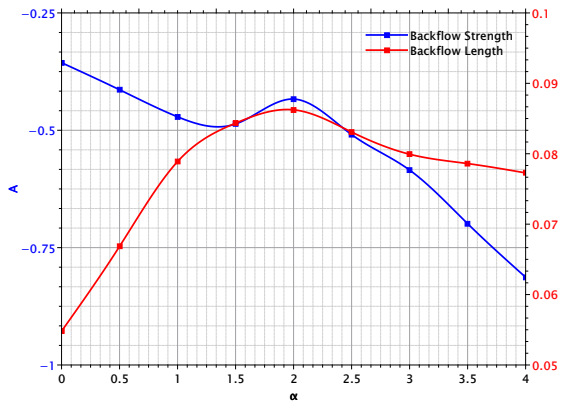


FIG. 6. Interaction power influence on the backflow parameters. Both - the backflow strength A (blue dots and interpolated spline) and length l (red dots and interpolated spline) - are present.

particles in the system.

An ideal case - single unit cell of a graphene quantum dot, separated largely enough to not be electronically connected, can be modelled well by a quantum harmonic oscillator, defined in Eq. 3. In comparison with monolayer graphene, which has been well studied [35, 36] for this purpose, this system yields stronger confinement in the ion sites, as is desired, and, hence, produces experimentally [18] better capacitance values. The parameters of this Hamiltonian can be estimated from the monolayer graphene [37] dispersion relation at the Γ point - the lowest energy point of the electron distribution - given by $E = \frac{3}{4}ta^2(k_x^2 + k_y^2) \rightarrow \frac{\pi^2 t}{9a^2}(x^2 + y^2)$ where $t = 2.8\text{eV}$ stems from nearest-neighbour tight-binding parameterization of the material and $a = 1.42\text{\AA}$ describes

the scale of the honeycomb lattice. The dielectric constant is taken that to be of monolayer graphene with $\epsilon = 5.7\epsilon_0$ as well. This results in an electron coupling constant of $\gamma = 0.83 \sim 1$, very similar to the simulations done above.

The capacitance can be obtained via

$$\mu = \frac{\epsilon_0}{\epsilon} \frac{dE}{dN}, \quad (15)$$

$$C_q = e \left(\frac{d\mu}{dN} \right)^{-1} = \frac{\epsilon e^2}{\epsilon_0} \left(\frac{d^2E}{dN^2} \right)^{-1}.$$

Here the voltage felt by the quantum dot is actually screened by the medium and, hence, has to be reduced $\frac{\epsilon}{\epsilon_0}$ times. The presence of the second order energy derivative signifies that quite sensitive observable measurements, as can be done here, are required due to the mainly linear nature of the energy dependence, visible in Fig. 4. The respective quantum capacitance calculation, at room temperature was obtained from fitting this energy data to a third order polynomial curve. An additional comparison to the experimentally measured total capacitance values can be calculated as well and it can be seen that the quantum capacitance estimate $C_q \approx 1400 \mu\text{F cm}^{-2}$ is an order bigger than the experimentally measured total capacitance $C \approx 100 \mu\text{F cm}^{-2}$ with a very minor linear dependence on the applied voltage. Hence, it is possible to further suggest that a more optimal quantum dot supercapacitor can be, potentially, made by balancing contributions of the quantum C_q and electrolyte double-layer C_e capacitances more evenly. This is due to their inverse contribution to the total capacitance via

$$C = \frac{C_q C_e}{C_q + C_e}. \quad (16)$$

Hence, ideally $C_e \sim C_q$ is desired. This, roughly fifteenfold, decrease of the quantum capacitance can be most easily achieved by further developments of the current ongoing work [38] on doping the graphene oxide precursor or, otherwise, using different materials, to increase the dielectric screening of the material.

IV. CONCLUSION

We have shown that the simple hydrodynamic backflow transformation significantly reduces the Fermion sign problem in path integral molecular dynamic simulations of a harmonically trapped two-dimensional electron gas at finite temperature. It has been studied [11, 12] to house a very rich, fractal nodal structure, with a changing amount of nodes, and, as well, shown to crystallize out in variational and diffusion quantum Monte-Carlo studies of various systems. Given that the computational cost of evaluating a Fermionic wavefunction is known to

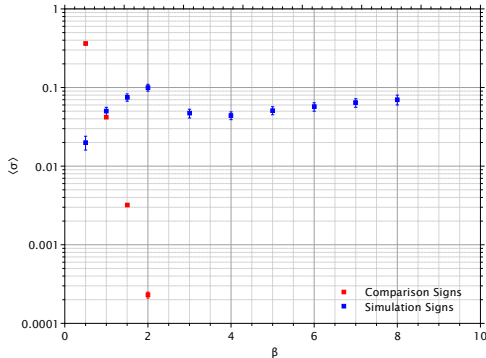


FIG. 7. Sign values (blue dots) with the corresponding errors for different temperatures from the backflow transformed simulation runs. A partial comparison (red dots) with previous study data of Dornheim [15] with no applied backflow is given as well.

be caused by the complex - heavily alternating - structure of its nodal surface, these backflow functions, hence, form an ideal basis functions for mitigating this problem

Our first attempt to optimise parameters of these backflows was a continuous normalizing flow machine learning approach which was found to reduce the relative error of the total energy, approximately, three times at medium sign severity, from $\langle\sigma\rangle \approx 0.2$ to $\langle\sigma\rangle \approx 0.5$ respectively. Overall, whilst we could learn directly from the simulation examples, the method was inefficient, numerically unstable and brittle.

We therefore developed a semi-analytic approach to directly optimise the backflow parameters with the aid of a closed-form solution for first order improvement of the sign, and used this as a gradient in a standard numeric optimisation. The resulting transformations, agreed, where possible, with the previous continuous normalizing flows approach and were found to reduce the problem by multiple orders of magnitude at more severe cases, with the sign value reaching $\langle\sigma\rangle = 0.07 \pm 0.01$ at minimum. The total energy of the system matched with previous, backflow untransformed, studies and energies for up to 32 electrons were calculated, in comparison to the currently possible system size of 10 electrons. A possible Wigner crystallization phase transition at 16 trapped particles was found, as well, from a bump in the energy and, more significantly, in the sign dependence curve. In addition, the Lindemann criteria was calculated to match quite closely at 18 particles. The limiting factor was found to be, primarily, the $O(N^3)$ calculation of the Jacobian, stemming from the coordinate transformation of the backflow and a more thorough implementation was suggested to further improve this scaling.

Finally, as a specific practical use case in energy storage systems, the quantum capacitance for graphene quantum dot materials was calculated.

V. ACKNOWLEDGEMENT

The authors gratefully acknowledge fruitful discussions with Matthew Foulkes and Frank Kruger. J.M.F. is a Royal Society University Research Fellow (URF-R1-191292). I.V. is supported by a Royal Society doctoral studentship from the same grant. The authors gratefully acknowledge access to computing resources provided by the Imperial College Research Computing Service [39]. Derivations in this work, were carried out with the help of the Mathematica [40] symbolic manipulation software.

Appendix A: Neural Network Approach

Each of the PIMD simulations, used for learning, were run separately with a unique random number generator seed and a single sign value and particle bead configuration extracted for the learning process. This was done in order to remove auto-correlation effects and random generator seed dependence as much as possible and yielded an average sign value of $\langle\sigma\rangle \approx 0.2$ for the backflow untransformed case, as seen in Fig. 8. Additionally, an energy value of $E \approx 13$ was obtained, hence both observable values being in agreement with the original study [5] as well. Note that the optimal size of the simulation dataset was estimated to be $N = 128$ by looking at the convergence of the average sign $\langle\sigma\rangle$, displayed in Fig. 8, with respect to its size.

In order to further perform minimization for the learning process, a step size of 10^{-3} was used together with the *AdamW* solver and it was stopped when the relative difference of the cost function reached 10^{-5} between steps. The learning process itself required a careful approach, since any significant instability would just produce a backflow representing a constant coordinate shift of the whole simulation independent of the sign, meaning that no nodal structure had been extracted. Hence, in order to remedy this, the neural networks were first trained on a very small dataset size of $N = 4$ and, further, the weights of these networks were used as an initial guess to converge them for higher dataset sizes of, first, $N = 16$ and, finally, $N = 128$ sizes. Additionally, the neural networks $\{A_n(\sigma, T)\}$ and $\{l_n(T)\}$ themselves were found to be of satisfactory composition with one hidden linear class layer and four neurons, enough to describe a few cycles of a $\sin(x)$ trigonometric function with relative deviations within a percent. More complex forms were found to introduce instabilities in the learning process and not yield a better description of the backflows at the same time.

In the case of a single backflow, the learned strength scale is displayed in Fig. 9 with respect to the sign. It can be seen that the zero intercept of the strength scale approximately crystallizes out the average sign value of the untransformed simulation $\langle\sigma_0\rangle \approx 0.2$, as previously discussed and expected. The strengths can be seen to be dependent on the sign with a form similar to the *tanh*

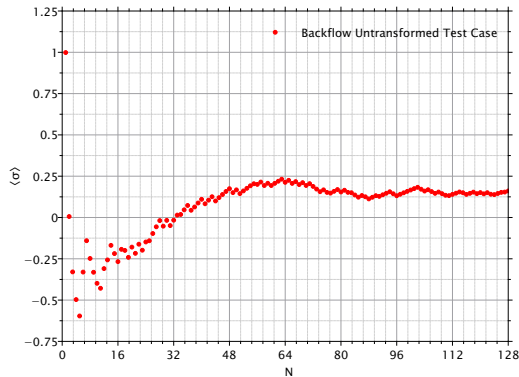


FIG. 8. Convergence of the average sign (red dots) with respect to the size of the backflow untransformed simulation dataset.

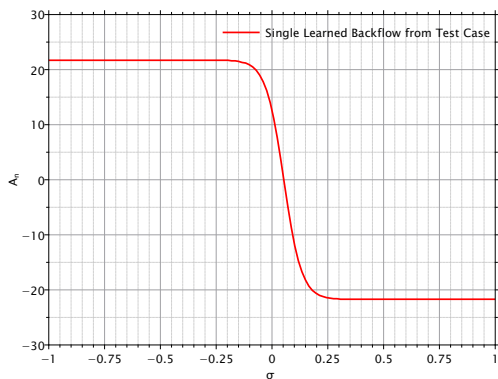


FIG. 9. Learned backflow transformation strength scale dependence on the sign in the case of a single backflow.

function, which is most likely due to the fact that the sign values of the individual samples tend to be either $\sigma \approx \pm 1$ and not often anything in between.

Moving on, this backflow was implemented on top of the stochastic path integral ring polymer molecular dynamics software. Specifically, the *RelativeDistance* and *Distance* functions - gateways, in code, between any stored coordinate space values and observable, in-

cluding gradient, calculations - were modified using Eq. 7 in order to make the simulation sample the backflow transformed coordinate space with a strength of $A_1(T = 1.0, \sigma = 1.0) = -15.83$ and scale $l_1(T = 1.0) = 0.05374$. This did require a decrease of the time step to $h = 0.00125$ - half its original value, otherwise most of the simulation runs would fail. This yielded an average sign value of $\langle \sigma \rangle \approx 0.5$, in a very similar fashion as in Fig. 8, and an energy value of $E \approx 13$, hence agreeing with the energy value of the untransformed simulation dataset and showing an increased average sign value, signifying a better sampling of the Fermionic nodal surface. Note that, since the neural network $\{A_n(\sigma, T)\}$ has no bounds on σ , it was never expected for the simulation to yield the perfect average sign value of $\langle \sigma \rangle$ value of 1.0, but rather depict how to achieve its maximum value instead, as discussed previously.

The above learning process was repeated for the case of four backflows. One of these resulted in having negligible impact and the rest were of practically identical length $l_{1,2,3}(T = 1.0) \approx 0.0346$ and strength $A_{1,2,3}(T = 1.0, \sigma = 1.0) \approx -13.8$ scale characterization, hence showing that, in this case, a single backflow function is enough for obtaining the best sampling description of the Fermionic nodal surface. This fact is further supported by comparing both simulation strengths via $A_1 l_1^3 \approx A_1 l_1^3 + A_2 l_2^3 + A_3 l_3^3 + A_4 l_4^3$ which shows that both results yield the same coordinate transformation effect. This agrees with previous VMC studies [30] that used an arbitrary 8th order polynomial and, by energy minimization, found a result very similar to the form used here. In an interesting manner, the values of these four backflows yielded a slightly lower average sign value of $\langle \sigma \rangle \approx 0.4$, most probably caused by the noise from overrepresentation, in comparison with the single backflow case. A further direct grid sampling of varying length and strength scales is displayed in Fig. 1. It can be reaffirmed that the above stated values, represented by a blue dot, do indeed represent a maximum on the $\langle \sigma \rangle(A_1, l_1)$ map and it is interesting to note that at certain values the average sign value can actually become small and, therefore, be more costly to evaluate. It is expected that the small deviation from the simulation values, present in the figure, is caused by finite size effects, since 64 square bins were used here with approximately 128 simulation values of the average sign $\langle \sigma \rangle$ for each one. This was of identical amount to the previous discussion, summarized by Fig. 8, in order to achieve convergence.

-
- [1] D. M. Ceperley, Fermion nodes, *Journal of Statistical Physics* **63**, 1237 (1991).
 [2] W. E. Pickett, Colloquium: Room temperature superconductivity: The roles of theory and materials design, *Reviews of Modern Physics* **95**, 021001 (2023).
 [3] T. Dornheim, T. Doppner, P. Tolias, M. P. Bohme, L. B. Fletcher, T. Gawne, F. Graziani, D. Kraus, M. J. Mac-

- Donald, Z. A. Moldabekov, S. Schwalbe, D. O. Gericke, and J. Vorberger, Unraveling electronic correlations in warm dense quantum plasmas, *Nature Communications* **16** (2024).
 [4] B. Hirshberg, V. Rizzi, and M. Parrinello, Path integral molecular dynamics for bosons, *Proceedings of the National Academy of Sciences* **116**, 21445 (2019).

- [5] Y. Xiong and H. Xiong, On the thermodynamic properties of fictitious identical particles and the application to fermion sign problem., *The Journal of Chemical Physics* **157** **9**, 094112 (2022).
- [6] L. A. Thiede, C. Sun, and A. A. Guzik, Waveflow: Boundary-conditioned normalizing flows applied to fermionic wave functions, *APL Machine Learning* (2022).
- [7] S. Lawrence, A. Shelby, and Y. Yamauchi, Quantum states from normalizing flows, *arXiv* (2024).
- [8] H. Xie, L. Zhang, and L. Wang, Ab-initio study of interacting fermions at finite temperature with neural canonical transformation, *Journal of Machine Learning* **1**, 38 (2022).
- [9] D. Schuh, J. Kreit, E. Berkowitz, L. Funcke, T. Luu, K. A. Nicoli, and M. Rodekamp, Simulating correlated electrons with symmetry-enforced normalizing flows, *arXiv* (2025).
- [10] R. P. Feynman and M. Cohen, Energy spectrum of the excitations in liquid helium, *Physical Review* **102**, 1189 (1956).
- [11] N. Kaplis, F. Kruger, and J. Zaanen, Entanglement entropies and fermion signs of critical metals, *Physical Review B* **95**, 155102 (2016).
- [12] F. Kruger and J. Zaanen, Fermionic quantum criticality and the fractal nodal surface, *Physical Review B* **78**, 035104 (2008).
- [13] T. Q. Chen, Y. Rubanova, J. Bettencourt, and D. K. Duvenaud, Neural ordinary differential equations, in *Neural Information Processing Systems* (2018).
- [14] M. Holzmann, D. M. Ceperley, C. Pierleoni, and K. Esler, Backflow correlations for the electron gas and metallic hydrogen., *Physical Review E* **68**, 046707 (2003).
- [15] T. Dornheim, Fermion sign problem in path integral monte carlo simulations: Quantum dots, ultracold atoms, and warm dense matter., *Physical Review E* **100** **2-1**, 023307 (2019).
- [16] U. Merkt, J. Huser, and M. Wagner, Energy spectra of two electrons in a harmonic quantum dot., *Physical Review B* **43** **9**, 7320 (1991).
- [17] S. M. Reimann and M. Manninen, Electronic structure of quantum dots, *Reviews of Modern Physics* **74**, 1283 (2002).
- [18] S. Zhang, L. Sui, H. Dong, W. He, L. Dong, and L. Yu, High-performance supercapacitor of graphene quantum dots with uniform sizes., *ACS Applied Materials and Interfaces* **10** **15**, 12983 (2018).
- [19] Y. R. Kumar, K. Deshmukh, K. kumar Sadasivuni, and S. K. K. Pasha, Graphene quantum dot based materials for sensing, bio-imaging and energy storage applications: a review, *RSC Advances* **10**, 23861 (2020).
- [20] S. Lawrence and Y. Yamauchi, Convex optimization of contour deformations, *Physical Review D* (2023).
- [21] A. Alexandru, G. Basar, P. F. Bedaque, and N. C. Warrington, Complex paths around the sign problem, *Reviews of Modern Physics* **94**, 015006 (2022).
- [22] A. Alexandru, G. Basar, and P. F. Bedaque, Monte carlo algorithm for simulating fermions on lefschetz thimbles, *Physical Review D* **93**, 014504 (2015).
- [23] B. Hirshberg, M. Invernizzi, and M. Parrinello, Path integral molecular dynamics for fermions: Alleviating the sign problem with the bogoliubov inequality., *The Journal of Chemical Physics* **152** **17**, 171102 (2020).
- [24] T. Dornheim and Y. Yan, Abnormal quantum moment of inertia and structural properties of electrons in 2d and 3d quantum dots: an ab initio path-integral monte carlo study, *New Journal of Physics* **24** (2022).
- [25] A. Paszke, S. Gross, F. Massa, A. Lerer, J. Bradbury, G. Chanan, T. Killeen, Z. Lin, N. Gimelshein, L. Antiga, A. Desmaison, A. Kopf, E. Yang, Z. DeVito, M. Raison, A. Tejani, S. Chilamkurthy, B. Steiner, L. Fang, J. Bai, and S. Chintala, Pytorch: An imperative style, high-performance deep learning library, in *Advances in Neural Information Processing Systems* (2019).
- [26] I. Vitenburgs and J. M. Frost, [Hydrodynamic Backflow for Easing the Fermion Sign in Finite-Temperature Electron Path Integral Simulations](#), GitHub (2026).
- [27] J. Hermann, Z. Schätzle, and F. Noé, Deep-neural-network solution of the electronic schrödinger equation, *Nature Chemistry* , 1 (2019).
- [28] D. Pfau, J. S. Spencer, A. G. D. G. Matthews, and W. M. C. Foulkes, Ab initio solution of the many-electron schrödinger equation with deep neural networks, *Physical Review Research* **2**, 033429 (2020).
- [29] S. Lawrence and Y. Yamauchi, Normalizing flows and the real-time sign problem, *Physical Review D* (2021).
- [30] P. L. Rios, A. Ma, N. D. Drummond, M. D. Towler, and R. J. Needs, Inhomogeneous backflow transformations in quantum monte carlo calculations., *Physical Review E* **74**, 066701 (2006).
- [31] Y. Kwon, D. M. Ceperley, and R. M. Martin, Effects of three-body and backflow correlations in the two-dimensional electron gas., *Physical Review B* **48** **16**, 12037 (1993).
- [32] M. M. Taddei, M. Ruggeri, S. Moroni, and M. Holzmann, Iterative backflow renormalization procedure for many-body ground-state wave functions of strongly interacting normal fermi liquids, *Physical Review B* **91**, 115106 (2015).
- [33] A. Griewank and A. Walther, Evaluating derivatives - principles and techniques of algorithmic differentiation, second edition, in *Frontiers in Applied Mathematics* (2000).
- [34] S. A. Khrapak, Lindemann melting criterion in two dimensions, *Physical Review Research* **2**, 012040 (2020).
- [35] H. Xu, Z. Zhang, and L. Peng, Measurements and microscopic model of quantum capacitance in graphene, *Applied Physics Letters* **98**, 133122 (2011).
- [36] T. Fang, A. Konar, H. G. Xing, and D. Jena, Carrier statistics and quantum capacitance of graphene sheets and ribbons, *Applied Physics Letters* **91**, 092109 (2007).
- [37] A. H. C. Neto, F. Guinea, N. M. R. Peres, K. S. Novoselov, and A. Geim, The electronic properties of graphene, *Reviews of Modern Physics* **81**, 109 (2007).
- [38] Y. Xu, X. Li, G. Hu, T. Wu, Y. Luo, L. Sun, T. Tang, J. Wen, H. Wang, and M. Li, Graphene oxide quantum dot-derived nitrogen-enriched hybrid graphene nanosheets by simple photochemical doping for high-performance supercapacitors, *Applied Surface Science* **422**, 847 (2017).
- [39] Imperial College London, Research Computing Service, 10.14469/hpc/2232.
- [40] W. R. Inc., [Mathematica, Version 14.1](#), champaign, IL, 2024.